



## Effect of Additives on Shape Evolution during Electrodeposition

### III. Trench Infill for On-Chip Interconnects

Yan Qin,<sup>a,\*</sup> Xiaohai Li,<sup>a,\*</sup> Feng Xue,<sup>a</sup> Philippe M. Vereecken,<sup>a,\*\*,c</sup>  
Panayotis Andricacos,<sup>b</sup> Hariklia Deligianni,<sup>b,\*\*</sup> Richard D. Braatz,<sup>a,\*\*</sup> and  
Richard C. Alkire<sup>a,\*\*\*,z</sup>

<sup>a</sup>Department of Chemical and Biomolecular Engineering, University of Illinois at Urbana-Champaign,  
Urbana, Illinois 61801, USA

<sup>b</sup>IBM Thomas J. Watson Research Center, Yorktown Heights, New York 10598, USA

Experimental observations are reported on the range of compositions and geometries for which void-free “superfilling” of rectangular trenches occurs during copper electrodeposition from acid sulfate solutions containing poly(ethylene glycol), chloride, bis(sodium sulfopropyl)disulfide, and 1-(2-hydroxyethyl)-2-imidazolidine-thione. Observations were compared with predictions made with a model that included 17 species and reaction intermediates that participated in a network of 15 surface reactions as well as surface diffusion, and three homogeneous reactions. The numerical algorithm was designed to handle stiffness arising from reaction terms and computational efficiency required for interface movement. Accurately estimated values of the most sensitive model parameters were used to carry out simulations of shape evolution. One assumption was needed to bring the model into agreement with experimental trends for the “window” of superfilling conditions over the range investigated experimentally. Numerical results were found to track behavior typically observed during superfilling, such as an incubation period, bottom-up acceleration, and bump formation. Predictions of the distribution of adsorbed species during trench infill support the interpretation that superfilling arises from generation of a catalytic accelerator species within the trench in the presence of transport-limited competitive adsorption of suppressor and inhibitor additives.

© 2008 The Electrochemical Society. [DOI: 10.1149/1.2816282] All rights reserved.

Manuscript submitted August 23, 2007; revised manuscript received October 22, 2007. Available electronically January 22, 2008.

The fabrication of on-chip interconnects by electrodeposition of copper in high-aspect-ratio trenches and vias without forming voids, known as “superfilling,” involves the use of solution additives.<sup>1</sup> The operating conditions and solution compositions for which acceptable superfilling can be achieved may be expected to change as device sizes shrink and as new process demands emerge, e.g., new materials. To maintain the pace of technology innovation, improved engineering methodologies, validated by comparison with experimental data, are needed for predicting behavior associated with the design, scale-over, optimization, and control of additive-based electrodeposition processes. This work presents a comparison of experimental trench-fill data with numerical simulations of shape change in the presence of a complex, realistic additive system. The present work (Part III) builds on recently developed techniques for carrying out multiscale simulations of electrodeposition processes (Part I),<sup>2</sup> which span from molecular-scale aspects of additive behavior to feature-scale shape change during infill, and for estimating values of the most sensitive system parameters (Part II),<sup>3</sup> by analysis of experimental data on roughness evolution and electrochemical potential transients.

A recent review<sup>4</sup> of superconformal electrodeposition processes associated with formation of smooth surfaces for functional and/or decorative purposes provides a summary of various proposed mechanisms, which depend on the length scale of the surface features in question. Smoothing processes are usually associated with electrolyte additives that cause local inhibition or acceleration of the deposition rate. That work, as well as Parts I and II of this series, includes a summary of experimental observations of shape-evolution phenomena associated with superfilling of on-chip interconnects.

The role of additives during superfilling has been described qualitatively according to their role as accelerator, suppressor, or leveler. Understanding the underlying physical and chemical basis of the influence of additives on metal deposition kinetics, however, is challenging because of the presence of subtle synergistic effects

between them.<sup>4</sup> For copper superfilling applications, a well-characterized model system has emerged for the acid sulfate system which includes an “accelerator” [bis(3-sulfopropyl)disulfide, SPS], a “suppressor” [poly(ethylene glycol) with trace chloride, PEG and Cl], and an “inhibitor” [1-(2-hydroxyethyl)-2-imidazolidinethione, HIT]. A summary of possible reactions for this system has been reported.<sup>5</sup> In the present series of publication, a subset of those reactions has been proposed as a mechanism hypothesis in order to demonstrate the computational methods (see Table I in Part I, and Table II in Part II).

To briefly summarize the proposed mechanism, deposition proceeds by a two-step reduction of  $\text{Cu}_{\text{aq}}^{2+}$  on bare copper sites via soluble intermediate  $\text{Cu}_{\text{aq}}^+$  ions. Cu adatoms may move by surface diffusion on those open surface sites that are not occupied by other adsorbates. The “suppressor” mechanism occurs by formation of adsorbed  $\text{CuCl}_{\text{ads}}$  and subsequent combination with a  $\text{PEG}_{\text{aq}}$  molecule to form the suppressor  $\text{CuClPEG}_{\text{ads}}$  which blocks other reactions on its site. The “accelerator” mechanism proceeds by reduction of  $\text{SPS}_{\text{aq}}$  via a reaction network to generate  $\text{Cu(I)thiolate}_{\text{ads}}$ , which serves to catalyze  $\text{Cu}_{\text{aq}}^+$  reduction. The “leveler” mechanism occurs when  $\text{HIT}_{\text{aq}}$  displaces adsorbed  $\text{Cu(I)thiolate}_{\text{ads}}$  and thus acts as a catalyst poison. The proposed mechanism does not include all possible reactions among the solution species, neither does it take into consideration the presence of oxygen nor the transient building of breakdown- or side-products. Meanwhile, fundamental investigations on the various aspects of the overall system continue to be reported,<sup>6,7</sup> with the result that the mechanism used here represents a working hypothesis that may be refined as new understanding develops.

There is significant literature on mathematical modeling of shape evolution during electrodeposition and etching which has been developed for systems in which the surface processes were characterized by generalized adsorption/reaction steps.<sup>8-11</sup> Such approaches are useful for clarifying underlying fundamental principles. However, the current series (Parts I–III) is directed toward the growing demand for molecular engineering decision-making for which methodologies are needed to provide accurate predictions with known error bars for the design of complex practical systems for which fundamental understanding of scientific details is uncertain. Such advances will enable a new generation of molecular engineering methods and optimization algorithms for rapidly selecting the best

\* Electrochemical Society Student Member.

\*\* Electrochemical Society Active Member.

\*\*\* Electrochemical Society Fellow.

<sup>c</sup> Present address: IMEC v.z.w., 3001 Leuven, Belgium.

<sup>z</sup> E-mail: r-alkire@uiuc.edu

Table I. Test range of components in the electrolytic bath.

	Low	Middle	High
CuSO <sub>4</sub> (mol/L)	0.25	0.3	0.7
H <sub>2</sub> SO <sub>4</sub> (g/L)	5	125	175
SPS (ppm)	1	6–10	50
PEG (g/L)	0.1	0.3	1
Cl <sup>-</sup> (ppm)	10	50	100
HIT (ppb)	50	100	1000
Trench width (μm)	0.18		2
Trench depth (μm)	1		
Trench AR	5.6		0.5
Nominal current density (mA/cm <sup>2</sup> )	11.5		

physical design variables, initial conditions, startup procedures, set-point trajectories, and feedback control systems.<sup>12,13</sup>

In Parts I and II of the present series, new methods were reported for multiscale simulations for trench infill by copper electrodeposition and for estimation of physicochemical parameters based on experimental measurements of roughness evolution. It was found that although the multiscale simulation model has the capability of capturing complex surface chemistry and detailed information on roughness evolution, it was computationally expensive because of the presence of extremely fast events associated with surface diffusion in the KMC code. In Part III, experimental observations of the region where superfilling occurs are compared with numerical predictions made with the system parameters estimated previously, but with new numerical procedures that are more computationally efficient.

### Experimental

Experiments were performed with a rotating disk in solutions maintained at 25 ± 0.2°C in a water-jacketed cell. The rotation rate (300 rpm) was selected so that the nominal rate of electrodeposition was less than 10% of the mass-transfer-limiting current density of Cu<sup>2+</sup>. The working electrode consisted of a patterned wafer segment held in a Teflon holder (exposed area 0.71 cm<sup>2</sup>). The wafer (QC-DETC064, International Sematech) had a 100 nm Cu seed layer on a 25 nm Ta barrier layer. Features were etched into 1000 nm plasma-enhanced tetraethylorthosilicate on 100 nm plasma-enhanced chemical vapor deposited nitride over 5500 nm thermal oxide and Si substrate. The line-space reticle on the wafer included a range of trench widths between 0.18 and 2 μm having a fixed height of 1 μm. Investigations were carried out on feature widths between 0.18 and 0.3 μm, which corresponded to aspect ratios (ARs) (depth/width) of 3.3 to 5.6, respectively. The counter electrode was a Cu wire (99.95%, Alfa Aesar) and the reference electrode was mercury/mercurous sulfate [G0093, Koslow Instruments, 0.64 V vs saturated hydrogen electrode (SHE)].

Electrodeposition was carried out in solutions containing CuSO<sub>4</sub> (99.995%, Aldrich), H<sub>2</sub>SO<sub>4</sub> (99.999%, Aldrich), PEG (Mw 3400, Aldrich), Cl<sup>-</sup> added as HCl (Aldrich), SPS (Rohm and Haas Electronic Materials L.L.C., Shipley), and HIT (Rohm and Haas Electronic Materials L.L.C., Shipley). All experiments were conducted in constant current mode (Solartron 1286 ECI, Schlumberger; with CorrWare software, Scribner). To prevent dissolution of the Cu seed layer, electrolysis was started as soon as the working electrode was immersed into the electrolyte (biased immersion). Table I summarizes the range of experimental conditions that were investigated.

After experiments, the wafer fragments were frozen by liquid nitrogen and broken to expose cross sections of the trenches, which were examined by scanning electron microscopy (Hitachi S-4700). For every feature size, more than 50 trenches were examined to determine the filling results. Additional experimental details are available elsewhere.<sup>14</sup>

### Simulation Procedures

Here we describe the components of a multiscale model including transport and reactions in the solution and at the interface, the movement of the interface, code coupling, and implementation of constant current conditions. Most of these components were described in Part I of this series, while the parameter values used here were obtained by procedures described in Part II. Although the kinetic Monte Carlo simulation used in Parts I and II was found to capture complex surface chemistry and detailed information of surface morphology, it was computationally expensive, as noted previously, due to surface diffusion. In Part III, the KMC component of the multiscale simulation code was replaced with a more computationally efficient module which used a set of differential equations to describe the reaction rate equations. To enable the constant current simulation as described in Part I, a controller is designed to manipulate the applied potential to achieve the constant current. Detailed discussion of the simulation procedure is available elsewhere.<sup>15</sup>

### Mathematical Model

*Transport and reaction in the electrolytic solution.*— The model uses a dilute solution description<sup>16</sup> of the transport and reaction of species *i* in the electrolytic solution

$$\frac{\partial C_i}{\partial t} = -\bar{\nabla} \cdot \bar{N}_i + A_i^{\text{soln}} = \bar{\nabla} \cdot (D_i \bar{\nabla} C_i) + \bar{\nabla} \cdot (z_i F u_i C_i \bar{\nabla} \Phi) + A_i^{\text{soln}},$$

$$i = 1, \dots, I_p \quad [1]$$

The net production rate of solution species *i* can be expressed as a function of the concentrations of solution species

$$A_i^{\text{soln}} = \xi_i(C_1, C_2, \dots, C_{I_p}) = \sum_{j=J_p+1}^{J_a} s_{ij}^{\text{soln}} r_j^{\text{soln}}(C_1, C_2, \dots, C_{I_p}) \quad [2]$$

where (*J<sub>a</sub> - J<sub>p</sub>*) is the total number of homogeneous reactions in the electrolytic solution. The boundary conditions at the top of the electrolytic solution are

$$C_i = C_i^\infty \quad [3]$$

$$\Phi = \Phi^\infty \quad [4]$$

The boundary conditions on the sides are

$$\bar{N}_i \cdot \bar{\mathbf{n}} = J_i \quad [5]$$

where the flux of species *i* is described by

$$\bar{N}_i = -D_i \bar{\nabla} C_i - z_i u_i F C_i \bar{\nabla} \Phi \quad [6]$$

For nonactive boundaries and symmetric boundaries *J<sub>i</sub>* = 0. For active boundaries *J<sub>i</sub>* is a function of concentrations, overpotential, and surface coverage of surface species

$$J_i = \psi_i(C_1, C_2, \dots, C_{I_p}, \theta_{I_p+1}, \theta_{I_p+2}, \dots, \theta_{I_a}, \Phi) = \sum_{j=1}^{J_p} s_{ij}^{\text{surf}} r_j^{\text{surf}} \quad [7]$$

where *J<sub>p</sub>* is the total number of surface reactions at the metal/electrolyte interface. In addition, the electroneutrality condition holds

$$\sum_{i=1}^{I_p} z_i C_i = 0 \quad [8]$$

The above equations form a system of coupled nonlinear partial differential and algebraic equations.

*Propagation of the metal/electrolyte interface.*— The level-set method (LSM)<sup>17</sup> is used to track the motion of the metal/electrolyte

interface. The LSM has proven to be a highly robust and accurate method for tracking moving interfaces. The level-set equation describing the interface evolution is

$$\phi_t + \bar{v} \cdot \bar{\nabla} \phi = 0 \quad [9]$$

If the interface is locally moving in the normal direction, i.e.,  $\bar{v} = \bar{\mathbf{n}}v$ , Eq. 9 becomes

$$\phi_t + v|\bar{\nabla} \phi| = 0 \quad [10]$$

The normal vector and the curvature of the metal/electrolyte interface are easily expressed in terms of the level-set function

$$\bar{\mathbf{n}} = \frac{\bar{\nabla} \phi}{|\bar{\nabla} \phi|} \quad [11]$$

$$\kappa = \bar{\nabla} \cdot \bar{\mathbf{n}} = \bar{\nabla} \cdot \left( \frac{\bar{\nabla} \phi}{|\bar{\nabla} \phi|} \right) \quad [12]$$

*Transport and reaction at the metal/electrolyte interface.*— Although the kinetic Monte Carlo code used in Parts I and II of this series has the capability of computing surface roughness evolution, it was computationally expensive because of the presence of extremely fast events associated with surface diffusion. Therefore, as described in detail in Part II and elsewhere,<sup>18</sup> once accurate estimates of the parameter values were obtained, a simpler code was utilized to explore the effect of a variety of operating conditions on the transient surface coverage of adsorbed species, and the transient surface concentration of solution species at the inner edge of the mass-transfer diffusion layer. The simpler code represents the spatially localized surface reactions with a set of differential equations, given in Table II of Part II. The limitation of this approach is that aspects of the system associated with surface roughness cannot be addressed.

The mass transport of surface species (except copper) on the propagating metal/electrolyte interface can be written as

$$\frac{\partial(L\theta_i\Pi_i)}{\partial t} + \bar{\nabla} \cdot (\bar{v}L\theta_i\Pi_i) = LA_i^{\text{surf}}, \quad i = Ip + 1, \dots, Ia \text{ on } \Gamma \quad [13]$$

where  $L$  is the length of the tangent vector along the metal/electrolyte interface ( $L = \sqrt{\phi_x^2 + \phi_y^2}$ ), and  $\Pi_i$  is the surface density of surface species  $i$  ( $\Pi_i = 1/N_A d_i^2$ ). Equation 13, which is defined only on the metal/electrolyte interface, describes how the change of surface coverage arises from the movement of the metal/electrolyte interface and surface reactions. The net production rate of surface species  $i$  is given by

$$A_i^{\text{surf}} = \zeta_i(C_1, C_2, \dots, C_{Ip}, \theta_{Ip+1}, \theta_{Ip+2}, \dots, \theta_{Ia}, \Phi) = \sum_{j=1}^{Jp} s_{ij}^{\text{surf}} r_j^{\text{surf}} \quad [14]$$

where  $Jp$  is the total number of surface reactions. If the interface is locally moving in the normal direction, then  $\bar{v} = \bar{\mathbf{n}}v$  and this equation becomes

$$\frac{\partial\theta_i}{\partial t} + v\bar{\nabla} \cdot (\bar{\mathbf{n}}\theta_i) = \frac{A_i^{\text{surf}}}{\Pi_i} \text{ on } \Gamma \quad [15]$$

or

$$\frac{\partial\theta_i}{\partial t} + v\bar{\mathbf{n}} \cdot \bar{\nabla}\theta_i = \frac{A_i^{\text{surf}}}{\Pi_i} - B_i v \kappa \theta_i \text{ on } \Gamma \quad [16]$$

where  $\bar{\mathbf{n}}$  and  $\kappa$  are given by Eq. 11 and 12, respectively, and the constant  $B_i$  is an adjustable constant which was set by trial-and-error, as described below, to a value of 50 for Cu(I)thiolate<sub>ads</sub> and to 1 for all other species. For the detailed derivation of Eq. 13 and 15,

readers are referred to Ref. 19. The surface coverage of copper (species  $s$ ) is then

$$\theta_s = 1 - \sum_{\substack{i \in [Ip+1, Ia] \\ i \neq s}} \theta_i, \quad s \in [Ip + 1, Ia] \quad [17]$$

## Numerical Methods

*Level-set framework.*— The level-set equation can be reformulated as

$$\phi_t + v_{\text{ext}}|\bar{\nabla} \phi| = 0 \quad [18]$$

where  $v_{\text{ext}}$  is the extension of  $v$  obtained by using the fast marching method (FMM).<sup>17</sup> The velocity  $v$  is only defined on the metal/electrolyte interface, while  $v_{\text{ext}}$  is defined over the computational domain and matches  $v$  on the metal/electrolyte interface. Similarly, Eq. 16 can be recast to the computational domain

$$\frac{\partial\theta_{i,\text{ext}}}{\partial t} + v_{\text{ext}} \left( \frac{\bar{\nabla} \phi}{|\bar{\nabla} \phi|} \cdot \bar{\nabla}\theta_{i,\text{ext}} \right) = \frac{A_{i,\text{ext}}^{\text{surf}}}{\Pi_i} - v_{\text{ext}} \left( \bar{\nabla} \cdot \left( \frac{\bar{\nabla} \phi}{|\bar{\nabla} \phi|} \right) \right) \theta_{i,\text{ext}} \quad [19]$$

where  $\theta_{i,\text{ext}}$ , analogous to  $v_{\text{ext}}$ , is the extension of  $\theta_i$  and matches  $\theta_i$  on the metal/electrolyte interface. The values of  $\theta_{i,\text{ext}}$  can be also constructed from  $\theta_i$  by using the FMM.

*Coupled level set-finite volume method.*— Equations 1 and 8 can be solved with the finite volume method.<sup>2</sup> The wide range of reaction rates causes numerical stiffness associated with the reaction term  $A_i^{\text{soln}}$  in Eq. 1 and  $A_{i,\text{ext}}^{\text{surf}}$  in Eq. 19. A fractional-step method was therefore used by which Eq. 19 was solved in two stages

$$\frac{\partial\theta_i}{\partial t} = \frac{A_i^{\text{surf}}}{\Pi_i} \text{ on } \Gamma \quad [20]$$

$$\frac{\partial\theta_{i,\text{ext}}}{\partial t} + v_{\text{ext}} \left( \frac{\bar{\nabla} \phi}{|\bar{\nabla} \phi|} \cdot \bar{\nabla}\theta_{i,\text{ext}} \right) = -v_{\text{ext}} \left( \bar{\nabla} \cdot \left( \frac{\bar{\nabla} \phi}{|\bar{\nabla} \phi|} \right) \right) \theta_{i,\text{ext}} \quad [21]$$

Equation 20, which is only defined on the metal/electrolyte interface, was solved with Eq. 1 and 8 using a stiff decay method (the backward differentiation formula method) for time stepping; then Eq. 21 takes the resulting value of  $\theta_i$  as the initial conditions.

A multilevel grid was used as in Part I, i.e., a fine grid is used for solving Eq. 18 and 21, and a coarse grid for solving Eq. 1, 9, and 20. This approach gave improved accuracy while reducing computational cost. The algorithmic procedure was:

Initialization: Given an initial metal/electrolyte interface  $\Gamma^0$ , construct  $\phi$  as a signed distance function. Given initial surface coverage  $\theta_i^0$  of surface species, extend to the computational domain as  $\theta_{i,\text{ext}}^0$ .

Loop: Given  $C^n$ ,  $\Phi^n$ ,  $\phi^n$ ,  $\theta_{i,\text{ext}}^n$ :

1. Calculate  $C^{n+1}$ ,  $\Phi^{n+1}$ , and  $\hat{\theta}^{n+1}$  (Eq. 1, 8, and 20).
2. Calculate the propagating rate of the interface  $v$  and extend it to the computational domain  $v_{\text{ext}}$ . Extend  $\hat{\theta}_i^{n+1}$  to the computational domain  $\hat{\theta}_{i,\text{ext}}^{n+1}$ . Interpolate the values of  $C^{n+1}$ ,  $\Phi^{n+1}$ ,  $\hat{\theta}^{n+1}$  if a fine grid is used in solving Eq. 18 and 21.
3. Calculate  $\phi^{n+1}$  and  $\theta^{n+1}$  (Eq. 18 and 21). Interpolate the values of  $\phi^{n+1}$  and  $\theta^{n+1}$  if a coarse grid is used in solving Eq. 1, 8, and 20.
4. Go to step 1 and repeat.

## Results and Discussion

Experimental observations of trench infill are presented below for a range of solution compositions, trench geometries, and deposition rates in order to identify conditions under which superfilling was found to occur. Results are compared with numerical simulations carried out with the hypothesized additive reaction mechanism

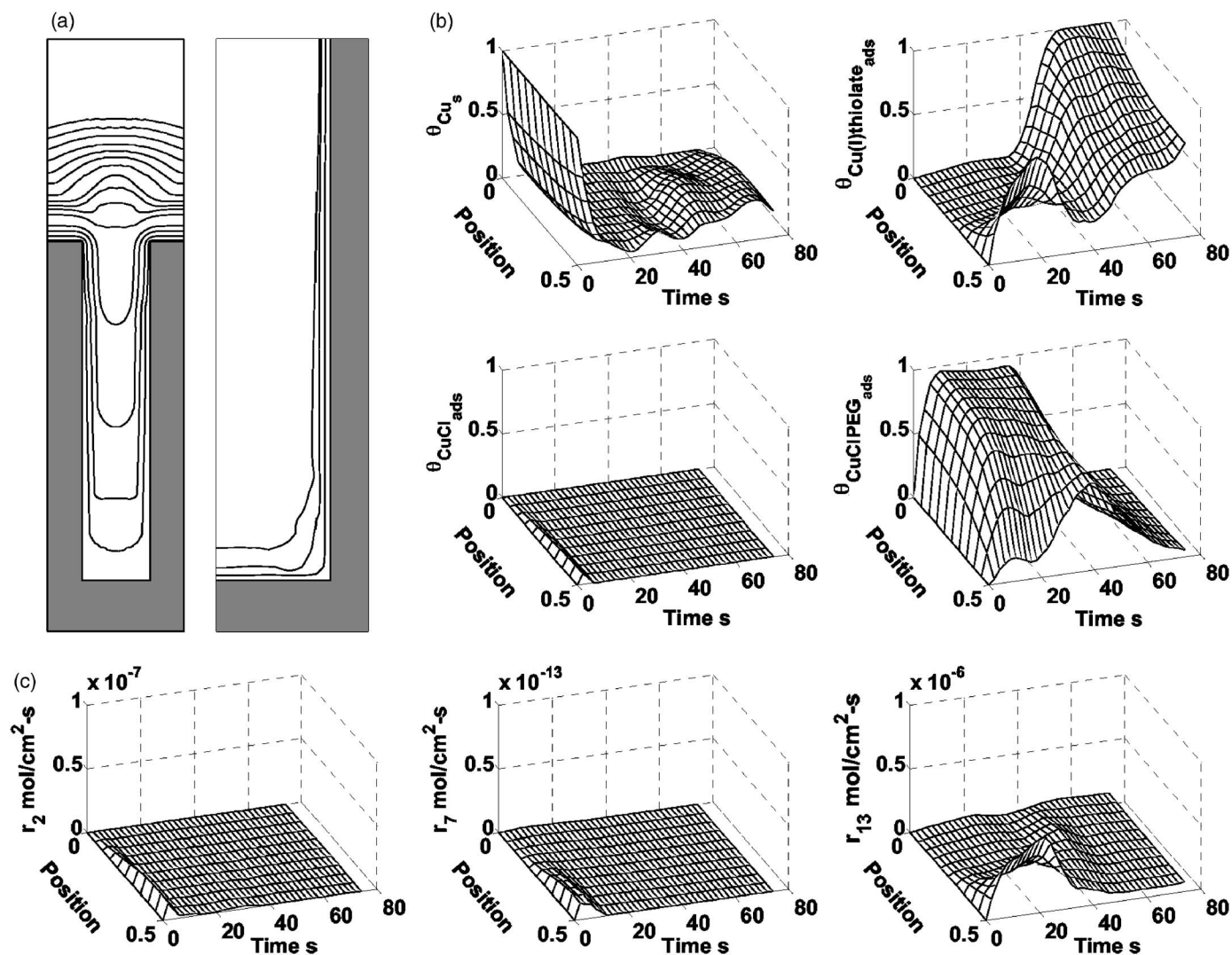


**Figure 1.** Simulation of trench infill with 0.3 M  $CuSO_4$ , 125 g/L  $H_2SO_4$ , 0.3 g/L PEG, 50 ppm  $Cl^-$ , and 10 ppm SPS; the trench is 0.2  $\mu m$  wide and 1  $\mu m$  high. (a) Two trench cross sections showing the shape evolution plotted (left) every 5 s for 0–70 s and (right) every 1 s for 0–3 s. (b) Four panels showing surface coverage vs time and position for four surface species during the trench infill. (c) Three panels showing the time-dependent reaction rate distribution for the three reactions associated with copper electrodeposition, i.e., Reactions 2, 7, and 13. The normalized arc length positions from 0 to 0.5 are positions along the propagating copper surface from the edge of the trench opening (0) and the center of the trench (0.5); i.e., moving along the lines profiles of (a) at a certain time from edge to center.

and the parameter values estimated from roughness evolution experiments as reported in Table VI of Part II of this series.<sup>3</sup> The numerical results could be brought into agreement with experimental data by adjusting  $B_{Cu(I)thiolate}$  to a value of 50. This adjustment serves to concentrate the  $Cu(I)thiolate_{ads}$  species at the region of highest curvature. All numerical results presented below were carried out with this adjustment. Numerical results are also reported below for the transient variation in local chemistry during trench infill.

**Superfilling.**— Numerical results are first presented for superfilling for a solution composition that is known from experiments reported in the literature to show the characteristic behavior of bottom-up superfilling and bump formation above the filled trench. The base case for initial discussion is 0.3 M  $CuSO_4$ , 125 g/L  $H_2SO_4$ , 0.3 g/L PEG (Mw 3400), 50 ppm  $Cl^-$ , and 10 ppm SPS in a trench 0.2  $\mu m$  wide by 1.0  $\mu m$  deep [(AR) = 5], and a nominal current density of 11.5 mA/cm<sup>2</sup>.

For the experiments reported here, the value of applied constant current was selected so as to give a current density in the range of 10–15 mA/cm<sup>2</sup> based on projected area, which is typical of indus-

trial practice. However, because the macroscopic pattern density of features on the test specimens used in this work was nonuniform, the actual local current density based on projected area was found to vary from place to place on the specimen.<sup>20</sup> The value of the local current used in comparing simulations with experimental data was therefore obtained directly from measurements of the copper deposit thickness observed in a time sequence of trench cross sections (not shown), with the assumption of 100% current efficiency for a two-electron reduction. For example, for the base-case conditions for experiments carried out with AR = 5, it was found that the local current density based on projected area was initially 75 mA/cm<sup>2</sup> and decreased to 15 mA/cm<sup>2</sup> after about 30 s when the trench filled. The applied current corresponding to those values was used for the simulations reported in Fig. 1. A similar procedure was used to determine the apparent local current for every instance of comparison between experiment and simulation.

**Incubation period.**— It is widely reported in numerous experimental studies cited in the introduction that the copper deposit within a trench grows initially at a uniform rate everywhere, after which the rate at the trench bottom accelerates rapidly (the “superfilling” ef-

**Table II. Species and reactions in copper electrodeposition.<sup>a</sup>**

<i>j</i>	Surface reactions
1	$\text{Cu}_{\text{aq}}^{2+} + \text{e}^- \rightarrow \text{Cu}_{\text{aq}}^+$
2	$\text{Cu}_{\text{aq}}^+ + \text{e}^- \rightarrow \text{Cu}_{\text{s}}$
3	$\text{Cu}_{\text{s}} \rightarrow \text{Cu}_{\text{aq}}^+ + \text{e}^-$
4	$\text{Cu}_{\text{s}} \rightarrow \text{Cu}_{\text{s}}$ (surface diffusion from one site to an adjacent site)
5	$\text{Cu}_{\text{aq}}^+ + \text{Cl}_{\text{aq}}^- \rightarrow \text{CuCl}_{\text{ads}}$
6	$\text{CuCl}_{\text{ads}} \rightarrow \text{Cu}_{\text{aq}}^+ + \text{Cl}_{\text{aq}}^-$
7	$\text{CuCl}_{\text{ads}} + \text{e}^- \rightarrow \text{Cu}_{\text{s}} + \text{Cl}_{\text{aq}}^-$
8	$\text{CuCl}_{\text{ads}} + \text{PEG}_{\text{aq}} \rightarrow \text{CuCIPEG}_{\text{ads}}$
9	$\text{CuCIPEG}_{\text{ads}} \rightarrow \text{CuCl}_{\text{ads}} + \text{PEG}_{\text{aq}}$
10	$\text{SPS}_{\text{aq}} + 2\text{e}^- \rightarrow 2\text{thiolate}_{\text{aq}}^-$
11	$\text{Cu}_{\text{aq}}^+ + \text{MPS}_{\text{aq}} \rightarrow \text{Cu(I)thiolate}_{\text{ads}} + \text{H}_{\text{aq}}^+$
12	$\text{Cu(I)thiolate}_{\text{ads}} + \text{H}_{\text{aq}}^+ \rightarrow \text{Cu}_{\text{aq}}^+ + \text{MPS}_{\text{aq}}$
13	$\text{Cu}_{\text{aq}}^+ + \text{Cu(I)thiolate}_{\text{ads}} + \text{e}^- \rightarrow \text{Cu(I)thiolate}_{\text{ads}} + \text{Cu}_{\text{s}}$
14	$\text{Cu(I)thiolate}_{\text{ads}} + \text{HIT}_{\text{aq}} \rightarrow \text{Cu(I)HIT}_{\text{ads}} + \text{MPS}_{\text{aq}}$
15	$\text{Cu(I)HIT}_{\text{ads}} + \text{H}_{\text{aq}}^+ + \text{e}^- \rightarrow \text{HIT}_{\text{aq}} + \text{Cu}_{\text{s}}$
<i>j</i>	Homogeneous reactions
16	$\text{MPS}_{\text{aq}} \leftrightarrow \text{H}_{\text{aq}}^+ + \text{thiolate}_{\text{aq}}^-$
17	$\text{H}_2\text{SO}_{4,\text{aq}} \leftrightarrow \text{HSO}_{4,\text{aq}}^- + \text{H}_{\text{aq}}^+$
18	$\text{HSO}_{4,\text{aq}}^- \leftrightarrow \text{SO}_{4,\text{aq}}^{2-} + \text{H}_{\text{aq}}^+$

<sup>a</sup> Electrochemical and chemical reactions on the surface. In this table, the subscript aq denotes aqueous species, ads denotes surface-adsorbed species, and s denotes solid Cu. CuCIPEG represents the Cl–Cu(I)–PEG complex, and Cu(I)thiolate represents the Cu(I)[–S(CH<sub>2</sub>)<sub>3</sub>SO<sub>3</sub>H] complex. Because of the uncertain solution chemistry of HIT, Cu(I)HIT is used to represent a complex formed between Cu(I) and HIT.

fect), followed by a period of overgrowth and “bump” formation above the filled trench. For parameter values corresponding to the base case, Fig. 1a provides numerical results for the evolution of shape profiles. Figure 1b illustrates corresponding values for the local surface coverage of four key surface species during the course of trench fill. Figure 1c shows the time-dependent distribution of the three reaction rates associated with copper electrodeposition by Reactions 2, 7, and 13 (defined in Table II). These results are similar to those presented in Fig. 6 and 7 of Part I, except that here the more accurate system parameters reported in Part II are used. The points made in the discussion of those previous results remain relevant for these new results.

Prior to the onset of deposition, all species in the solution within the trench are at their bulk concentrations. As seen in Fig. 1b, the surface consists initially of “bare” unoccupied Cu<sub>s</sub> sites, an assumption of the model, which rapidly become occupied by other adsorbed species. As current begins to flow, Cu<sub>aq</sub><sup>2+</sup> is reduced to Cu<sub>aq</sub><sup>+</sup>, followed by several possible reactions of the cuprous ions. For example, the figures in Fig. 1b illustrate the rapid adsorption of PEG<sub>aq</sub> via the formation of CuCl<sub>ads</sub> by Reaction 5 and CuCIPEG<sub>ads</sub> by Reaction 8. The PEG<sub>aq</sub> inside the trench (not shown) becomes rapidly depleted due to its low bulk concentration, fast adsorption rate, and low diffusion coefficient. As a consequence, PEG<sub>aq</sub> adsorbs preferentially near the trench opening, with a CuCIPEG<sub>ads</sub> coverage gradient along the trench sidewall.<sup>21</sup> Meanwhile, MPS, generated by Reactions 10 and 16, reacts with Cu<sub>aq</sub><sup>+</sup> to form Cu(I)thiolate<sub>ads</sub> at the base of the trench where there are available unoccupied sites. Figure 1b illustrates that the surface coverage of Cu(I)thiolate<sub>ads</sub> is initially low but that its coverage at the bottom of the trench increases steadily. Figure 1b also indicates that the CuCl<sub>ads</sub> coverage increases briefly within the trench (via Reaction 5) but is thereafter consumed and remains low throughout the process. The profiles shown in the right portion of Fig. 1a illustrate that trench infill follows a conformal growth pattern during the first few seconds, after which superfilling commences in the corner and then spreads over the bottom surface.

**Bottom-up acceleration.**— In Fig. 1a, the time sequence of shape profiles between 0 and 25 s has the trench filling rapidly with hardly any additional deposit growth on the exterior surface. The high rate constant found in Part II for Reaction 13 in the proposed mechanism is consistent with the view that Cu(I)thiolate<sub>ads</sub> catalyzes copper electrodeposition. Comparison of surface coverages of CuCIPEG<sub>ads</sub> and Cu(I)thiolate<sub>ads</sub> in Fig. 1b indicates that bottom-up acceleration is accompanied by a difference in surface coverage of CuCIPEG<sub>ads</sub> and Cu(I)thiolate<sub>ads</sub> between the top and the bottom of the trench. As copper fills the trench, the local area change leads to accumulation of Cu(I)thiolate<sub>ads</sub> at the bottom with a decrease in CuCIPEG<sub>ads</sub> coverage. With rapid diffusion of Cu<sub>aq</sub><sup>+</sup> along the trench and low CuCl<sub>ads</sub> coverage, the deposition rate is controlled by the distribution of Cu(I)thiolate<sub>ads</sub> and unoccupied Cu<sub>s</sub> sites on the surface. CuCIPEG<sub>ads</sub> coverage remains high along the upper trench sidewalls and top surface, but at the bottom of the trench, the surface coverage of Cu(I)thiolate<sub>ads</sub> increases to about 20× higher than on the exterior surface. As a result, the local Cu deposition rate at the bottom accelerates, and the deposit fills the trench more quickly than the sidewalls can advance inward.

**Bump formation.**— In the shape profiles in Fig. 1a, a bump centered over the trench is formed after it becomes filled at about 25 s (the center of the bump corresponds to a normalized arc length of 0.5 in the figure). The bump serves to increase the surface area, and thus the number of unoccupied sites. Comparison of numerical results in Fig. 1b indicates that about 20% of the sites at the center of the deposit remain unoccupied “bare Cu,” and that most of the surface is covered by Cu(I)thiolate<sub>ads</sub>. Furthermore, at 25 s, the coverage of Cu(I)thiolate<sub>ads</sub> is high over the trench and low over the external surface. As a consequence the deposit continues to grow at a faster rate over the trench than over the external surface, thereby enlarging the bump.

**Bump disappearance.**— The bump seen in Fig. 1a eventually becomes less pronounced. Figure 1b indicates that the surface coverage of Cu(I)thiolate<sub>ads</sub> in the center increases more slowly than on the shoulders, which eventually gives higher surface coverage of Cu(I)thiolate<sub>ads</sub> on the shoulders. The local area change associated with the expanding bump creates new unoccupied surface sites around the shoulders. These simulations suggest that unoccupied sites are more readily occupied by Cu(I)thiolate<sub>ads</sub> than by CuCIPEG<sub>ad</sub> due to the slow formation of CuCl<sub>ads</sub>.

**Reaction network.**— For the base-case composition, copper deposition may occur via Reactions 2, 7, and 13 (Table II). Figure 1c plots the rate of those reactions as a function of time and position along the trench wall. The deposition via Reaction 2 is seen to occur mainly in the interior of the trench, where there is less PEG to intercept the Cu<sup>+</sup> intermediate. Deposition via Reaction 7 occurs to a very small extent, no doubt because CuCl is strongly complexed by PEG. Deposition occurs mainly through Cu(I)thiolate (Reaction 13), initially at the bottom of the trench and later over the entire surface.

**Effect of copper sulfate and sulfuric acid electrolyte.**— Experimental observations on superfilling are summarized in Table III for the effect of CuSO<sub>4</sub> and H<sub>2</sub>SO<sub>4</sub> on superfilling for various geometries in solutions containing 0.3 g/L PEG(3400), 50 ppm Cl<sup>–</sup>, 10 ppm SPS, and 100 ppb HIT. This combination of additives was found to produce superfilling with minimum bump formation. For every point shown in Table III (as well as Table IV and Fig. 2), visual observations of ~50 trench cross sections were examined to determine the filling results. These qualitative results indicated that most additive combinations successfully filled trenches (solid black dots) with a width of 0.25 μm (AR 4.0), while only some combinations filled trenches at 0.18–μm (AR 5.6). Also, for trenches in the range of 0.18–0.2 μm, high-acid-concentration baths (85–175 g/L) performed better than low-acid baths (5–45 g/L). The concentration of CuSO<sub>4</sub> had a much smaller influence on trench-infill results.

**Table III. Trench-infill results for various combinations of CuSO<sub>4</sub> and H<sub>2</sub>SO<sub>4</sub>: (●) over 85% void-free fill; (⊗) over 30% but less than 85% void-free fill; and (○) less than 30% void-free fill or completely fail. Other fixed additives are 0.3 g/L PEG, 50 ppm Cl<sup>-</sup>, 10 ppm SPS, and 100 ppb HIT. The current density was 11.5 mA/cm<sup>2</sup>, and rotation rate was 300 rpm.**

CuSO <sub>4</sub> (M)	H <sub>2</sub> SO <sub>4</sub> (g/L)	Trench width (μm) (trench height fixed at 1 μm)			
		0.3–0.26	0.25–0.24	0.22–0.2	0.19–0.18
0.25	175	●	●	●	⊗
	5	⊗	○	○	○
	25	●	●	⊗	○
	45	●	●	⊗	⊗
	85	●	●	●	●
0.30	125	●	●	●	●
	175	●	●	●	●
	25	●	●	⊗	⊗
	45	●	●	●	⊗
	85	●	●	●	⊗
0.50	125	●	●	●	⊗
	175	●	●	●	●
	25	●	●	●	⊗
	45	●	●	●	⊗
	85	●	●	●	⊗
0.70	125	●	●	●	●
	175	●	●	●	●
	25	●	●	●	⊗
	45	●	●	●	⊗
	85	●	●	●	●

Table IV provides qualitative results for the effect on superfilling of several combinations of CuSO<sub>4</sub> – H<sub>2</sub>SO<sub>4</sub> composition, geometry, and SPS concentration. For high-acid solution (175 g/L), low SPS (12 ppm) gave better superfilling for 0.18–0.22 μm trenches than higher concentrations (24 and 36 ppm SPS). For the smallest width trenches the opposite result was found for low-acid solution (25 g/L): high SPS concentrations gave better results, although voids were usually found. Note that the proposed physicochemical mechanism in Table II cannot yet fully simulate the acid and cupric ion concentration dependence. For this, the mechanism needs to be refined with the acid dependence of suppressor complex formation, as was proposed recently.<sup>6</sup> To summarize, high acid gave better infill of small-width trenches. An advantage of low-acid (and thus low-conductivity) solutions may be seen at the wafer scale, by enabling a more uniform macroscopic current distribution.

*Effect of SPS accelerator.*— The experimental results displayed in Fig. 2 summarize qualitative visual observations on superfill found for a range of SPS concentrations and ARs when [PEG], [Cl<sup>-</sup>], and [HIT] were set at 0.3 g/L, 50 ppm, and 100 ppb, respectively. Void-free infill (black dots) was found in a region of parameter space that extended from 6 to 20 ppm SPS and up to an AR of 5.6. Outside of this range, voids were found and the deposit quality was considered to be marginal (squares) or unacceptable (open circles). These observations are consistent with the findings of

others.<sup>22</sup> Simulation results for the extremes of SPS concentrations (0, 0.01, and 1000 ppm) are given in Fig. 3a-c in which the surface coverage of CuCIPEG<sub>ads</sub> and Cu(I)thiolate<sub>ads</sub> are shown as a function of time and position along the trench wall surface. For the situations where SPS is 0 and 0.01 ppm with other variables set at the base-case values, it may be seen in Fig. 3a and b that the surface coverage of CuCIPEG<sub>ads</sub> is high throughout the entire trench-fill process, and that the generation of Cu(I)thiolate<sub>ads</sub> catalyst is significantly delayed by comparison with the base case for 10 ppm SPS shown in Fig. 1b. For 1000 ppm SPS, Fig. 3c indicates that the catalyst forms rapidly but the CuCIPEG does not stifle sidewall growth, with the result that there is not a sufficiently large difference between the surface coverage of Cu(I)thiolate<sub>ads</sub> at the bottom and at the surface to result in bottom-up superfilling. The experiments and simulations in Fig. 2 and 3 indicate that superfilling occurs only at intermediate SPS concentrations, and the simulations indicate that low and high values of SPS concentrations cause different reasons for failure.

**Table IV. Trench-infill results for high/low acid concentration: (●) over 85% void-free fill; (⊗) over 30% but less than 90% void-free fill; and (○) less than 30% void-free fill or completely fail. Other additive concentrations are fixed at 0.3 g/L PEG, 50 ppm Cl<sup>-</sup>, and 100 ppb HIT. The current density was 11.5 mA/cm<sup>2</sup>, and rotation rate was 300 rpm.**

CuSO <sub>4</sub> (M)/H <sub>2</sub> SO <sub>4</sub> (g/L)	SPS (ppm)	Trench width (μm) (trench height fixed at 1 μm)		
		0.25–0.24	0.22–0.2	0.19–0.18
0.3/175	12	●	●	●
	24	⊗	⊗	⊗
	36	○	○	○
0.5/25	12	●	⊗	○
	24	●	⊗	⊗
	36	●	⊗	⊗

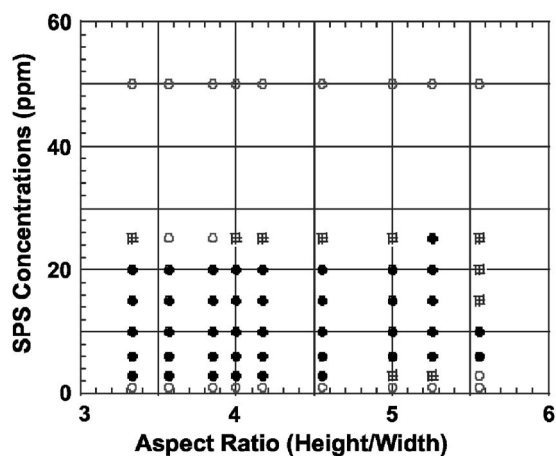


**Figure 2. Summary of experimental observations for the effect of SPS concentration and AR on trench infill with 0.3 M CuSO<sub>4</sub>, 125 g/L H<sub>2</sub>SO<sub>4</sub>, 0.3 g/L PEG, 50 ppm Cl<sup>-</sup>, and 100 ppb HIT: (●) more than 85% were void-free; (⊗) between 30 and 85% were void-free; and (○) less than 30% were void-free. All trenches are 1 μm high. For every feature size, more than 50 trenches were examined to determine the filling results.**

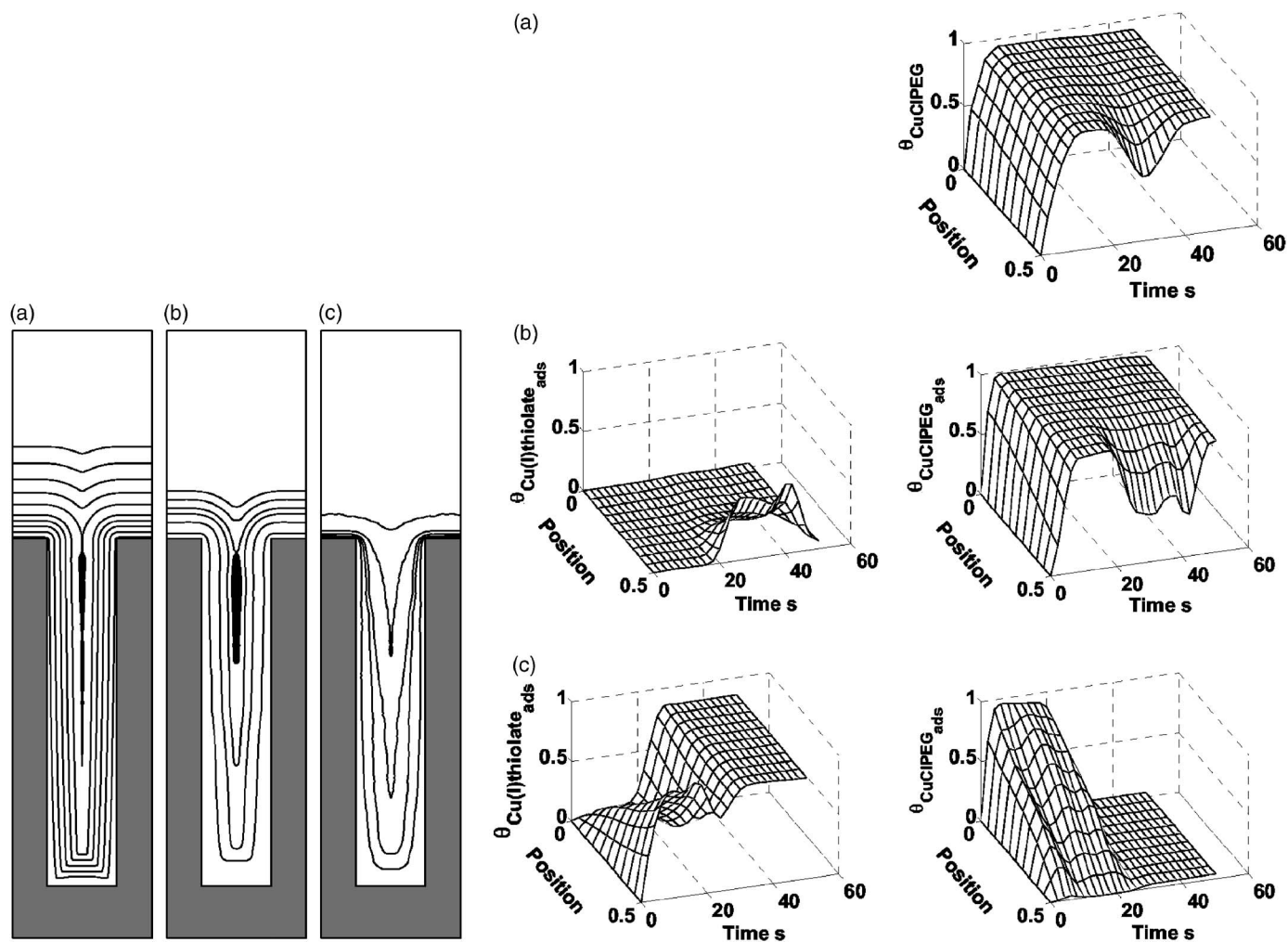


**Figure 3.** Simulations of the effect of SPS on trench infill with 0.3 M  $\text{CuSO}_4$ , 125 g/L  $\text{H}_2\text{SO}_4$ , 0.3 g/L PEG, 50 ppm  $\text{Cl}^-$ , and 100 ppb HIT; the trench is 0.2  $\mu\text{m}$  wide and 1  $\mu\text{m}$  high. Results are shown for three values of SPS concentration: (a) 0 ppm, (b) 0.01 ppm, and (c) 1000 ppm. (Left) Three trench cross sections showing the shape evolution plotted in every 5 s. (Right) Three panels showing surface coverage vs time and position for  $\text{Cu(I)thiolate}_{\text{ads}}$  and  $\text{CuCIPEG}_{\text{ads}}$  during the trench infill.

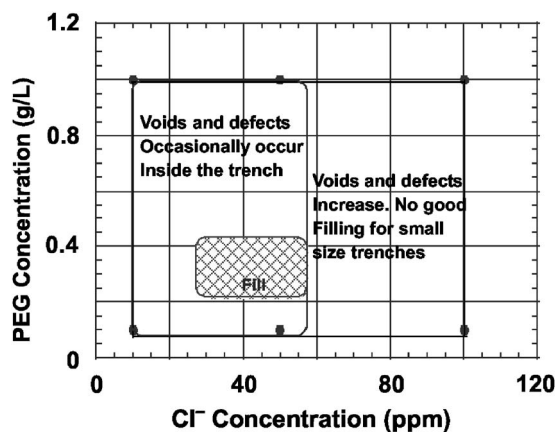


**Figure 4.** Summary of experimental observations for the effect of PEG and  $\text{Cl}^-$  concentration on trench infill with 0.3 M  $\text{CuSO}_4$ , 125 g/L  $\text{H}_2\text{SO}_4$ , and 10 ppm SPS. The cross-hatched rectangular region indicates the superfilling concentration range. Outside this region, voids were found to occur as indicated in the figure.

*Effect of poly(ethylene glycol)–chloride suppressor.*— Figure 4 illustrates qualitative experimental findings. The range of  $\text{PEG}_{\text{aq}}$  and  $\text{Cl}^-$  concentrations within which superfilling was observed was 0.2–0.4 g/L and 30–55 ppm, respectively. Deviations on either side of those concentration ranges were accompanied by randomly distributed voids in the trenches. With an overdose of  $\text{Cl}^-$ , voids appeared more often, especially for smaller trenches.

Numerical simulations carried out for low and high concentrations of PEG (0.1 and 1 g/L) are presented in Fig. 5. These results may be compared with corresponding results for the base case shown in Fig. 1, where  $[\text{PEG}] = 0.3$  g/L, and  $[\text{Cl}^-] = 50$  ppm. According to the proposed mechanism investigated here, PEG and  $\text{Cl}^-$  ions act in concert via the  $\text{CuCl}_{\text{ads}}$  species to impart a suppressing effect by  $\text{CuCIPEG}_{\text{ads}}$  adsorption. For low  $[\text{PEG}]$ , the coverage by  $\text{CuCIPEG}_{\text{ads}}$  near the trench opening is lower and the resulting  $\text{Cu(I)thiolate}_{\text{ads}}$  adsorption is higher; the difference in deposition rates between the top and bottom of the trench was insufficient to support superfilling. For high  $[\text{PEG}]$ , the  $\text{CuCIPEG}_{\text{ads}}$  coverage was so high that the onset of superfilling was not sustained. For both cases, the simulated profiles contained voids.

Numerical simulations carried out for low and high concentrations of  $\text{Cl}^-$  (10 and 100 ppm) also gave profiles that indicated void formation. For low values of  $\text{Cl}^-$ , the simulation results (not shown) indicated that PEG did not adsorb on the surface to function as the

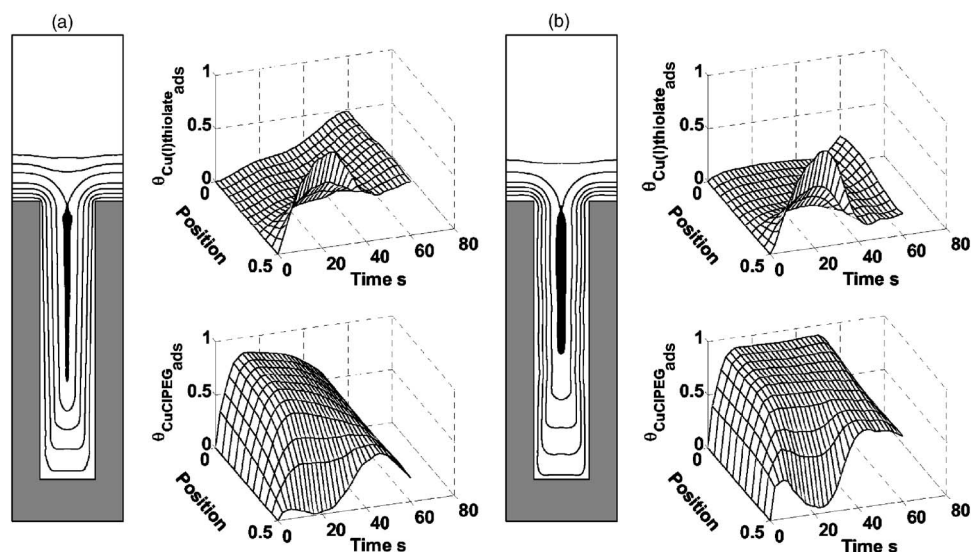


**Figure 5.** Simulations of the effect of PEG on trench infill with 0.3 M  $\text{CuSO}_4$ , 125 g/L  $\text{H}_2\text{SO}_4$ , 50 ppm  $\text{Cl}^-$ , 10 ppm SPS, and 100 ppb HIT; the trench is 0.2  $\mu\text{m}$  wide and 1  $\mu\text{m}$  high. Two groups of figures are shown for PEG concentrations of (a) 0.1 and (b) 1.0 g/L. Each group includes a trench cross section showing the shape evolution plotted every 5 s, and two panels showing surface coverage vs time and position for  $\text{Cu(I)thiolate}_{\text{ads}}$  and  $\text{CuCIPEG}_{\text{ads}}$  during the trench infill.

suppressor. For high values of  $\text{Cl}^-$ , superfilling was not sustained, with the result that voids appeared near the trench mouth.

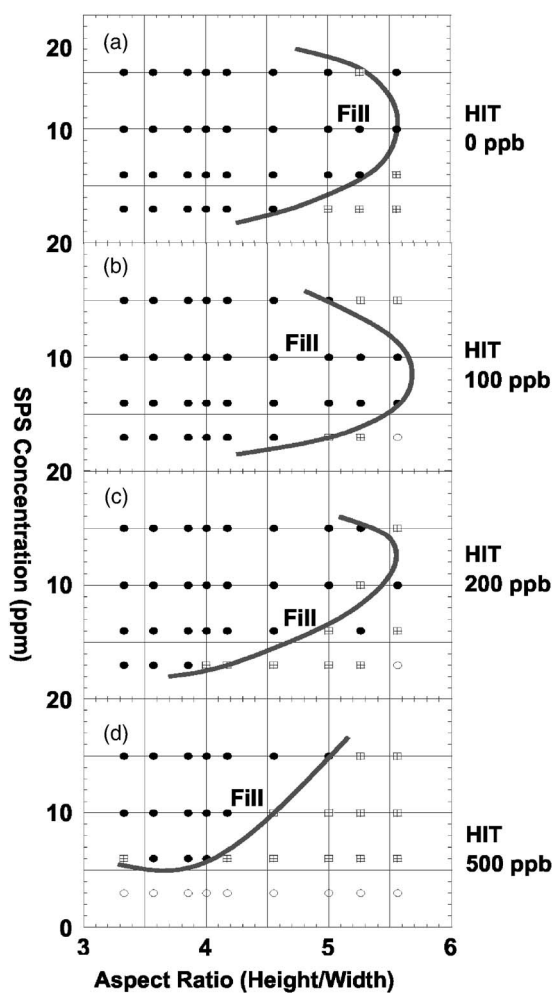


**Figure 6.** Summary of experimental observations for the effect of HIT and SPS concentrations on trench infill for various ARs with 0.3 M  $\text{CuSO}_4$ , 125 g/L  $\text{H}_2\text{SO}_4$ , 0.3 g/L PEG, and 50 ppm  $\text{Cl}^-$ : (●) more than 85% were void-free; (◐) between 30 and 85% were void-free; and (○) less than 30% were void-free. All trenches are 1  $\mu\text{m}$  high. For every feature size, more than 50 trenches were examined to determine the filling results.

*Effect of HIT leveler.*—Figure 6 summarizes experimental conditions for which HIT is effective in inhibiting bump formation for various SPS concentrations and ARs. It was found that HIT did not influence superfilling below a concentration of 100 ppb. On the contrary, it seems to promote infill somewhat for high ARs. However, for  $[\text{HIT}] \geq 500$  ppb, the ability to fill high-aspect-ratio trenches decreased with the formation of voids near the mouth of the trenches. The data also indicate that the range of HIT concentration over which superfilling occurs depends on SPS concentration. For an overdose of SPS, the voids appeared near the bottom of the trench, while for an overdose of HIT the voids were observed near the mouth. With too low an SPS concentration, the deposit surface was observed to become rough, which caused pinch-off voids between the sidewalls before the trench was completely filled. With the appropriate amounts of both SPS and HIT, bump formation could be reduced while the void-free trench-infill manner was still maintained. Within the feasible region, a higher HIT concentration was generally found to do a better job of eliminating the “overflow”.

Figure 7a shows a sequence of simulated trench profiles obtained with the base-case composition plus 200 ppb HIT; these results may be compared to those in Fig. 1a, which were obtained under otherwise identical conditions but without HIT. Bump formation did not occur with the 200 ppb HIT. Figure 7b plots surface coverage for various species. Comparison of Fig. 7b with Fig. 1b indicates that the presence of HIT serves to remove most of the  $\text{Cu(I)thiolate}_{\text{ads}}$  (by Reaction 14) within 40 s. Figure 7c plots the rate of copper deposition by HIT (Reaction 15); the reaction proceeds during early stages of trench fill, but because HIT is under mass-transfer control due to its low concentration, the reaction becomes starved. However, it does indicate that HIT does introduce a differential in copper deposition kinetics which could explain the slight beneficial effect on filling performance for high-aspect-ratio features observed in Fig. 6. As filling continues,  $\text{Cu(I)thiolate}_{\text{ads}}$  has to compete with suppressor for both cuprous ions and surface empty sites for Reactions 11 and 13 to proceed. As the trench fill nears completion, HIT becomes increasingly able to remove  $\text{Cu(I)thiolate}_{\text{ads}}$  and thus make possible the readsorption of  $\text{CuCIPEG}_{\text{ads}}$ , which serves also to decrease the unoccupied Cu sites. As the trench fill is completed, a sufficient quantity of  $\text{Cu(I)thiolate}_{\text{ads}}$  has accumulated that displaces the  $\text{Cu(I)CIPEG}_{\text{ads}}$ .

The experimental data (summarized in Fig. 6) indicate that an HIT concentration  $\geq 500$  ppb led to voids near the mouth of the trenches and the inability to fill small trenches. Numerical simula-

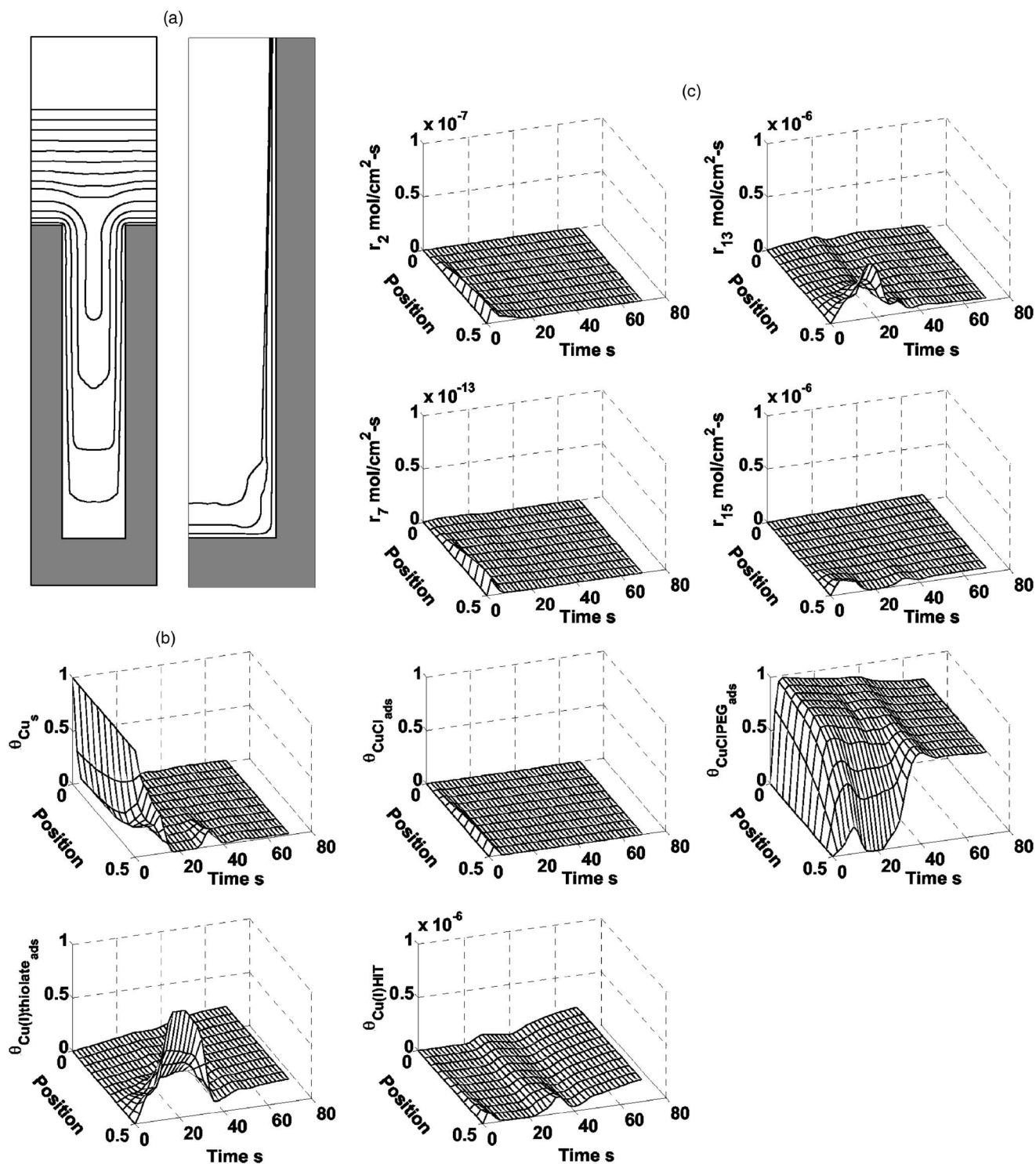


**Figure 7.** Simulations showing the effect of HIT on trench infill with 0.3 M  $CuSO_4$ , 125 g/L  $H_2SO_4$ , 0.3 g/L PEG, 50 ppm  $Cl^-$ , 10 ppm SPS, and 200 ppb HIT. The trench is 0.2  $\mu m$  wide and 1  $\mu m$  high. (a) Two trench cross sections showing the shape evolution plotted (left) every 5 s for 0–50 s and (right) every 1 s for 0–3 s. (b) Five panels showing surface coverage vs time and position for five surface species during the trench infill. (c) Three panels showing the time-dependent reaction rate distribution for the four reactions associated with copper electrodeposition by Reactions 2, 7, 13, and 15.

tions for  $[HIT] = 1000$  ppb (not shown) indicated that voids appeared near the trench mouth because the difference in  $Cu(I)thiolate_{ads}$  coverage between the top and the bottom was insufficient to drive superfilling. In addition, experimental data indicate that the effective range of HIT depends on SPS concentration. The effective range for HIT was larger for higher SPS concentrations. Simulation results (not shown) gave the result that superfilling could

be obtained with 500 ppb HIT and 15 ppm SPS ( $AR = 5$ ), while voids were found from simulations carried out with less than 15 ppm SPS.

### Conclusion

Experimental observations on whether superfilling occurred were carried out on rectangular trenches ( $AR$  3.3–5.6, width 180–300 nm)

for a range of electrolytic solutions containing  $\text{CuSO}_4$  (0.25–0.7 M),  $\text{H}_2\text{SO}_4$  (5–175 g/L), SPS (1–50 ppm), PEG (0.1–1 g/L),  $\text{Cl}^-$  (10–100 ppm), and HIT (50–1000 ppb) (Table II). For the case of 180 nm trench widths, superfill was observed experimentally in experiments with 0.3 g/L PEG, 30–55 ppm  $\text{Cl}^-$ , 6–15 ppm SPS, and 100–200 ppb HIT. High-acid electrolyte (85–175 g/L  $\text{H}_2\text{SO}_4$ ) gave a wider range of superfilling behavior than low-acid electrolyte (5–45 g/L  $\text{H}_2\text{SO}_4$ ). Over the range studied, variation in the  $\text{CuSO}_4$  concentration had a relatively small effect on superfilling results (Table III).

Experimental data on superfilling were compared with simulations based on a multiscale model that included the hypothesized physicochemical mechanism (Table II). An improved multiscale model for reaction, transport, and shape evolution was presented that has lower computational cost than the method used in Part I of this series. The principal features of the numerical method are (i) a level-set framework to track the metal/electrolyte interface and describe the mass balance of surface species on propagating interface, (ii) a finite volume method that uses a fixed Cartesian grid over an irregular domain to account for mass transport of solution species in electrolyte solution, and (iii) a coupling algorithm that can effectively handle numerical stiffness introduced by the rate equations.

Numerical simulations of deposit shape evolution during trench infill, carried out for the range of variables investigated experimentally, were found to require one adjustment to the model (i.e., setting  $B_{\text{Cu(I)thiolate}} = 50$ ) in order to simulate superfilling for the hypothesized mechanism with the parameters obtained in Part II. More recent results on predictions of superfilling without the adjustment of  $B_{\text{Cu(I)thiolate}}$  will be described in future publications. The numerical results reported here demonstrate agreement with the stages of superfilling which have been widely reported in the literature, namely, an incubation period followed by bottom-up acceleration and, in some cases, bump formation (Fig. 1). The simulation results provide predictions of the time and position dependence of the surface coverage of adsorbed species within the trench during infill, the current distribution, and the rate of copper deposition by the four routes associated with the proposed physicochemical mechanism (via  $\text{Cu}^+$ ,  $\text{CuCl}$ ,  $\text{Cu(I)thiolate}$ , and  $\text{Cu(I)HIT}$ , i.e., Reactions 2, 7, 13, and 15, respectively).

The superfill range for SPS was found experimentally between 6–20 ppm for  $\text{AR} = 3.3$ – $5.6$  with an electrolyte containing 0.3 g/L PEG, 30–55 ppm  $\text{Cl}^-$ , and 100–200 ppb HIT (Fig. 2). If SPS concentration was below 3 ppm, pinch-off voids were observed in the middle of the trench caused by conformal growth and roughening of the sidewall surface. With an overdose of SPS, trench infill resulted in voids and seams. Numerical simulations show the same trend as the experimental observations.

The superfill concentration range for PEG and  $\text{Cl}^-$  was found by experiments to be 0.2–0.4 g/L and 30–55 ppm, respectively (Fig. 4). For concentrations outside this region, voids occurred frequently (Fig. 4). Numerical simulations over these ranges were in agreement with both the superfill region and the formation of voids outside that region (Fig. 5).

A strong synergistic effect on superfilling was observed experimentally between SPS and HIT (Fig. 6). The feasible concentration range of leveler HIT depends on the concentration of SPS. Within the feasible range, a high HIT concentration was found to be effective in slowing the bottom-up growth rate as well as either delaying, decreasing the size, or eliminating altogether the formation of a bump. Voids near the trench mouth were observed when an excessive amount of HIT was added.

The hypothesized chemical mechanism in Table II involves a dynamic relationship between mass transport and surface reaction of the additives. One adjustment to the model was needed to simulate superfilling for the hypothesized mechanism with the nominal parameter values reported in Part II of this series. In addition, the model does not account for the acid dependence of the suppressor complex adsorption. The evaluation of refined and/or alternative hy-

potheses of mechanism may be carried out with the procedures reported in Parts I–III of this series. A number of insights into the proposed explanation for the superfilling process were obtained from the predicted time and position dependence of the surface coverage of adsorbed species, the individual reaction rate distributions, and the overall current distribution during trench fill (Fig. 1, 3, 5, and 7). According to the proposed mechanism investigated here, SPS acts as an accelerator by leading to the formation of  $\text{Cu(I)thiolate}_{\text{ads}}$  on the surface, which catalyzes electrodeposition. Within the appropriate range of concentration, the catalyst promotes bottom-up shape evolution by creating a difference between the growth rates at the bottom and at the opening of the trench due to the high coverage of  $\text{Cu(I)thiolate}_{\text{ads}}$  at the bottom, and low coverage near the trench opening. If the concentration of SPS is too low (Fig. 3), then the bottom growth rate is not fast enough to achieve superfilling.  $\text{PEG}_{\text{aq}}$  adsorbs following formation of  $\text{CuCl}_{\text{ads}}$ , which tethers  $\text{CuClPEG}_{\text{ads}}$  at the surface. The  $\text{PEG}_{\text{aq}}$  within the trench is rapidly depleted with preferential adsorption at the trench opening, creating a  $\text{CuClPEG}_{\text{ads}}$  coverage gradient along the trench sidewall. Meanwhile, the proposed mechanism indicates that MPS, generated by Reactions 10 and 16, reacts with  $\text{Cu}_{\text{aq}}^+$  to form  $\text{Cu(I)thiolate}_{\text{ads}}$  catalyst at the base of the trench where there are available unoccupied sites. According to the proposed mechanism, HIT introduces a species that forms complexes with  $\text{Cu}_{\text{aq}}^+$  that serve to displace  $\text{Cu(I)thiolate}_{\text{ads}}$ . The HIT concentration must be sufficiently low that the formation of HIT complexes occurs under mass-transport control, but not so low as to fail to displace  $\text{Cu(I)thiolate}_{\text{ads}}$ . Under proper conditions, the displacement of  $\text{Cu(I)thiolate}_{\text{ads}}$  by HIT primarily occurs not at the early stage when the thiolate catalyst is critical for superfilling, but at the later stage when the  $\text{Cu(I)thiolate}_{\text{ads}}$  is exerting the unwanted effect of bump growth. In these early stages, HIT shortly provides an alternative deposition route at the bottom of the trench through adsorbed  $\text{Cu(I)HIT}_{\text{ads}}$ .

The emphasis of this series of publications has been to establish improved multiscale simulation algorithms and systems tools to allow for the deep integration of computational investigation with experimental studies. Electrodeposition with additives provides a challenging application that involves uncertainties in the chemical mechanism, difficulties in making direct experimental observations, synergy between multiple phenomena that operate on different time and length scales, and the demand for timely transfer of new knowledge into rapidly evolving industrial practice. The simulation tools developed in this series are reusable and may be applied to other applications beyond the superfilling example used here for their initial development. Examples include many systems where control of events at multiple length scales is critical to product quality, and where molecular-scale events could be treated as the design focus in developing new products that exploit self-assembly during processing.

#### Acknowledgments

The authors acknowledge heartfelt appreciation for the contributions made to this paper by the late Dr. Andricacos. Funding for this work was provided by an IBM Faculty Partnership, the Frederick Seitz Material Research Laboratory Central Facilities (partially supported by the U.S. Department of Energy, grant DEFG02-91-ER45439, via the University of Illinois), the National Science Foundation under grants CTS-0135621 and CTS-0438356, and the National Computational Science Alliance under computing resource allocation NRAC MCA-01S022. Experimental work received support from the Semiconductor Research Corporation via SRC BEP 834. Any opinions, findings, and conclusions or recommendations expressed in this material are those of the authors and do not necessarily reflect the views of the National Science Foundation.

*The University of Illinois at Urbana-Champaign assisted in meeting the publication costs of this article.*

## List of Symbols

$A_i^{\text{soln}}$	production rate of solution species $i$ due to bulk reactions, M/s
$A_i^{\text{surf}}$	production rate of surface species $i$ due to surface reactions, mol/cm <sup>2</sup> s
$A_{i,\text{ext}}^{\text{surf}}$	extension production rate of surface species $i$ , mol/cm <sup>2</sup> s
$B_i$	adjustable constant in Eq. 16, set to 50 for Cu(I)thiolate <sub>ads</sub> and 1 for all other species
$C_i$	concentration of species $i$ , M
$C_i^\infty$	bulk concentration of species $i$ , M
$d_i$	diameter of the molecule, m
$D_i$	diffusion coefficient of species $i$ , cm <sup>2</sup> /s
$F$	Faraday's constant, $9.65 \times 10^4$ C/equiv
$I_a$	total number of species
$I_p$	total number of solution species
$J_i$	flux of species $i$ in the normal direction, mol/cm <sup>2</sup> s
$J_a$	total number of reactions
$J_p$	total number of surface reactions on the metal/electrolyte interface
$L$	length of the tangent vector along the metal/electrolyte interface, cm
$\bar{n}$	normal direction of the metal/electrolyte interface
$\bar{N}_i$	flux of species $i$ , mol/cm <sup>2</sup> s
$r_j^{\text{soln}}$	reaction rate of bulk reaction $j$ , mol/cm <sup>3</sup> s
$r_j^{\text{surf}}$	reaction rate of surface reaction $j$ , mol/cm <sup>2</sup> s
$R$	universal gas constant, 8.314 J/mol K
$s_{ij}^{\text{soln}}$	stoichiometric coefficient of species $i$ in bulk reaction $j$
$s_{ij}^{\text{surf}}$	stoichiometric coefficient of species $i$ in surface reaction $j$
$T$	absolute temperature, 298 K
$u_i$	mobility of species $i$ , $D_i/RT$ , cm <sup>2</sup> mol/J s
$v$	propagating velocity of the metal/electrolyte interface in the normal direction
$v_{\text{ext}}$	extension velocity
$\bar{v}$	propagating velocity of the metal/electrolyte interface
$z_i$	charge number of species $i$
Greek	
$\phi$	level-set function
$\Phi$	potential in solution, V
$\Phi^\infty$	potential on the top boundary, V
$\kappa$	curvature of metal/electrolyte interface
$\Gamma$	metal/electrolyte interface
$\theta_i$	surface coverage of species $i$
$\theta_{i,\text{ext}}$	extension surface coverage of species $i$
$\Pi_i$	surface density of surface species $i$ , mol/cm <sup>2</sup>
$s_i$	

function for calculating  $r_i^{\text{surf}}$   
 $\psi_i$  function for calculating  $r_i^{\text{soln}}$

## References

1. P. C. Andricacos, C. Uzoh, J. Dukovic, J. Horkans, and H. Deligianni, *IBM J. Res. Dev.*, **42**, 567 (1998).
2. X. Li, T. O. Drews, E. Rusli, F. Xue, Y. He, R. D. Braatz, and R. C. Alkire, *J. Electrochem. Soc.*, **154**, D230 (2007).
3. E. Rusli, F. Xue, T. O. Drews, P. Vereecken, P. Andracacos, H. Deligianni, R. D. Braatz, and R. C. Alkire, *J. Electrochem. Soc.*, **154**, D584 (2007).
4. T. P. Moffat, in *Advances in Electrochemical Science and Engineering*, R. Alkire, D. Kolb, J. Lipkowsky, and P. Ross, Editors, Vol. 10, VCH-Wiley Publishers, Weinheim (2007).
5. P. M. Vereecken, R. A. Binstead, H. Deligianni, and P. C. Andricacos, *IBM J. Res. Dev.*, **49**, 3 (2005).
6. J. G. Long, P. C. Searson, and P. M. Vereecken, *J. Electrochem. Soc.*, **153**, C258 (2006).
7. S. Bae and A. A. Gewirth, *Langmuir*, **22**, 10315 (2006).
8. R. Alkire, T. Bergh, and R. L. Sani, *J. Electrochem. Soc.*, **125**, 1981 (1978).
9. R. Sautebin, H. Froidevaux, and D. Landolt, *J. Electrochem. Soc.*, **127**, 1096 (1980).
10. J. O. Dukovic, in *Advances in Electrochemical Science and Engineering*, H. Gerischer and C. Tobias, Editors, Vol. 3, p. 117, Wiley & Sons, New York (1994).
11. M. Georgiadou, D. Veyret, R. L. Sani, and R. C. Alkire, *J. Electrochem. Soc.*, **148**, C54 (2001).
12. R. D. Braatz, R. C. Alkire, E. Seebauer, E. Rusli, R. Gunawan, T. O. Drews, X. Li, and Y. He, *J. Process Control*, **16**, 193 (2006).
13. D. G. Vlachos, A. B. Mhadeshwar, and N. S. Kaisare, *Comput. Chem. Eng.*, **30**, 1712 (2006).
14. Y. Qin, Ph.D. Thesis, University of Illinois at Urbana-Champaign, Urbana, IL (2006).
15. X. Li, Ph.D. Thesis, University of Illinois at Urbana-Champaign, Urbana, IL (2007).
16. J. S. Newman, *Electrochemical Systems*, p. 241, Prentice-Hall, Englewood Cliffs, NJ (1991).
17. J. A. Sethian, *Level Set Methods and Fast Marching Methods*, Cambridge University Press, New York (1999).
18. E. Rusli, Ph.D. Thesis, University of Illinois at Urbana-Champaign, Urbana, IL (2006).
19. D. Adalsteinsson and J. A. Sethian, *J. Comput. Phys.*, **185**, 271 (2003).
20. R. Akolkar and V. Dubin, *Electrochem. Solid-State Lett.*, **10**, D55 (2007).
21. R. Akolkar and U. Landau, *J. Electrochem. Soc.*, **151**, C702 (2004).
22. T. P. Moffat, D. Wheeler, C. Witt, and D. Josell, *Electrochem. Solid-State Lett.*, **5**, C110 (1999).